# Occurrence of dynamic strain aging in intercritically annealed low carbon high aluminum medium manganese steels

Shahroz Ahmed [a],[*], Jani Penttilä [a], Jari Rämö [a], Mari Honkanen [b], Veli-Tapani Kuokkala [a], Olli Oja [c], Pasi Peura [a]

[a] Engineering Materials Science, Faculty of Engineering and Natural Sciences, Tampere University, Tampere, Finland
[b] Tampere Microscopy Center, Tampere University, Finland
[c] SSAB Europe Oy, Hämeenlinna, Finland

## ARTICLE INFO

## ABSTRACT

Medium manganese steel grades heat treated with the quench and partition (Q&P) treatment have shown promising results of strength and formability, but the number of studies on high aluminum medium manganese Q&P steels still remains rather limited. Consequently, this study investigates the mechanical properties, behavior and microstructures of a low carbon-high aluminum medium manganese (3%) steel after intercritical annealing and subsequent Q&P heat treatments with varying heat treatment parameters. Samples that were intercritically annealed above 760 °C showed an ultimate tensile strength (UTS) of around 1500 MPa with uniform elongation values of approximately 10%. On the other hand, the samples annealed at 740 °C showed somewhat lower UTS values (in the range of 1000 … 1200 MPa) but much higher uniform and total elongations, i.e., considerably improved formability. However, the stress-strain curves of the samples annealed at 740 °C showed rather severe serrations that can be connected to the dynamic strain aging (DSA) phenomena, which limits the usability of the steel especially in applications where good surface quality of the deformed (sheet) is required. Therefore, the main focus of this article is on the samples annealed at temperatures close to $A_1$, where DSA serrations tend to appear. The evidence gathered from these investigations leads to the conjecture that the DSA serrations are due to the free carbon and nitrogen originating from the dissolution of M(C,N) and $M_2$(C,N) type carbides, which were formed during the intercritical annealing at temperatures producing less than 50% of the austenite phase. Other reasons for the occurrence of DSA in the current test materials can be the scarcity of martensite and the morphology of the retained austenite.

## 1. Introduction

To reduce carbon emissions and to ensure passenger safety, the automobile sector increasingly favors the use of lighter and stronger steels in many of the vehicle components. This demand has led to the development of new 'generations' of advanced high strength steels (AHSS). The current 'third generation' of AHSS includes, for instance, medium manganese steels, carbide free bainitic (CFB) steels, and quench and partition (Q&P) steels [1].

Quenching and partitioning is a heat treatment process that has been investigated in particular by Speer and co-workers, who in 2005 published an overview and progress report of the process [2]. In short, the Q&P heat treatment cycle consists of full or partial austenitization, followed by interrupted quenching between the martensite start temperature ($M_s$) and the martensite finish temperature ($M_f$), and partitioning above $M_s$. The process takes advantage of carbon partitioning from martensite to austenite, which lowers the $M_s$ temperature, thereby stabilizing austenite to room temperature (RT). The kinetics of carbon partitioning from martensite to austenite are described for example by Speer et al. [3]. In another investigation, Speer et al. [4] also developed a model, which estimates the fraction of retained austenite after partitioning as a function of the quenching temperature. The model assumes full partitioning of carbon from martensite to austenite and neglects the formation of carbides. The model uses the $M_s$ temperature and martensite transformation equations to predict the final austenite fraction. Several researchers have used this model successfully to predict the retained austenite content in the final microstructure at room temperature after the Q&P treatment [5–7].

Since the invention of the Q&P treatment, different steel grades have been examined for their microstructure and properties by modifying the Q&P process parameters. For example, both fully and partially austenitized low-to-medium carbon steels with different Mn contents have been investigated after the Q&P treatments [8–13]. Seo et al. [14] conducted Q&P heat treatments using varying quench temperatures to investigate the effect of the quench temperature on the microstructure and mechanical properties of a 4% Mn steel. They concluded that the amount of retained austenite and its carbon content depend on the martensite fraction formed during quenching. The effects of varying partitioning times and temperatures on the Q&P heat treatment outcomes have also been quite widely reported in the literature. For example, Ayenampudi et al. [15] applied the Q&P heat treatment to a medium manganese (4.5%) steel using different temperatures and concluded that, at the partitioning temperature of 450 °C, carbide precipitation can take place, but if the partitioning temperature is between 500 °C and 600 °C, pearlite can form. Hajyakbary et al. [16], in turn, reported the formation of carbide free bainite at the partitioning temperature of 400 °C, when the quenching temperature was between 220 °C and 260 °C and the partition time was over 50 s. Recent studies conducted on low carbon high aluminum steels [12,13] show that these steels offer good combinations of strength and ductility when heat treated with proper Q&P parameters. However, studies related to the intercritical annealing of low carbon-high aluminum medium manganese (3%) steels close to the $A_1$ transformation temperature are limited, and therefore more investigations are needed to better understand the microstructures, mechanical properties and behavior following from the application of the Q&P heat treatment after the intercritical annealing of steels in this temperature range.

In a tensile test conducted at a constant crosshead or piston displacement rate, sometimes 'serrations', appearing as irregular load drops or vibrations in the obtained stress-strain curve, can be observed. This phenomena is commonly known as the Portevin Le-Chatelier (PLC) effect, which is caused by the non-steady plastic flow due to the localization of plastic deformation into the so-called deformation or PLC bands [17–19]. The localized plastic deformation and the generation of the deformation bands, in turn, are associated with the dynamic strain aging (DSA) effect [20–22].

Rodriguez [20] explained the condition for load or stress drops in a tensile test with the following simple equation:

$$\dot{\varepsilon} = \dot{\varepsilon}_p + \frac{1}{E_s} \dot{\sigma} \qquad (1)$$

where $\dot{\varepsilon}$ is the total (imposed) strain rate, $\dot{\varepsilon}_p$ is the plastic strain rate in the specimen, $\dot{\sigma}$ is the stress rate in the specimen at any instant of time, and $E_s$ is the elastic modulus of the specimen-machine system. At any instant of time, when the plastic strain rate $\dot{\varepsilon}_p$ in the specimen momentarily exceeds the imposed strain rate $\dot{\varepsilon}$, the load in the testing system (and consequently the stress in the specimen) must drop to keep Equation (1) fulfilled. Rodriguez [20] further explained the different types of serrations caused by DSA and coined them as A, B, C, D and E types of DSA, as depicted in Fig. 1. The five types of DSA can be briefly described as follows [20]:

i. The A type DSA serrations are termed 'periodic locking and unlocking serrations'. Each serration corresponds to the initiation of a deformation band at the same end of the specimen, which then propagates over the length of the specimen and causes the sample to deform. When the band reaches the end of the sample, the sample continues to deform by the initiation of a new deformation band and the cycle continues.

ii. The B type DSA serrations are seen as fine oscillations in the stress-strain curve, arising from the discontinuous propagation of the deformation band due to DSA of the moving dislocations inside the band.
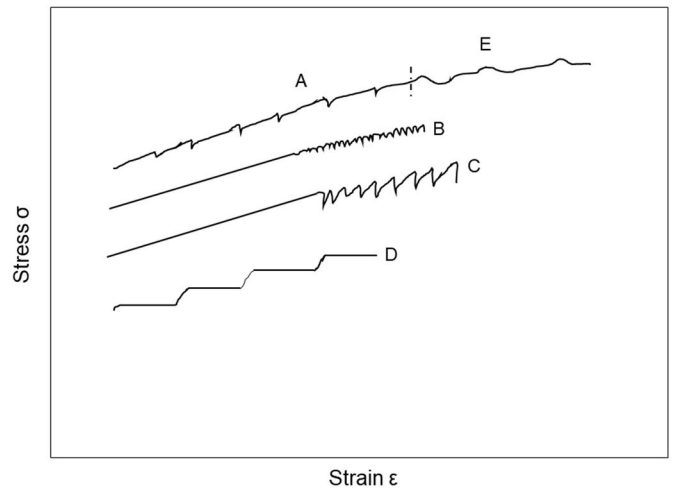


**Fig. 1.** Types of DSA serrations (adopted from Ref. [20]).

iii. The C type serrations occur at higher temperatures and lower strain rates than the A and B types, and are seen as yield drops below the general level of the stress-strain curve.

iv. The D type DSA appears as plateaus or stairs in the plastic flow curve, developing from the deformation band propagation with little to no work hardening. In the literature, quite little has been reported about the occurrence of the D type DSA.

v. The A type DSA can change to E type DSA at high strains. The E type serrations are similar to the A type, but with no work hardening taking place during the band propagation.

Although several explanations have been presented for the occurrence of DSA at the atomic level, none of them has been conclusively confirmed and the topic still remains debatable. The first theory related to the DSA effect was presented by Cottrell [23], according to which the dislocations interact with the interstitial solute atoms (such as C and N) in a solid solution. The interstitial solute atoms impede the movement of dislocations, which eventually become pinned in the regions of solute atoms. When sufficient stress builds up and the pinned dislocations overcome the critical energy barrier to continue their movement, rapid unpinning of dislocations occurs. This alternating rapid pinning and unpinning of dislocations is seen as load or stress drops in the stress-strain curve, i.e., as the PLC effect. The interstitial atom atmospheres where the dislocations become pinned are commonly known as the Cottrell clouds.

The motion of dislocations is discontinuous, or 'jerky', during plastic deformation, i.e., the dislocations become temporarily stopped at the obstacles and then break free and continue their glide along the slip path [24]. The condition for the occurrence of DSA is based on the 'arrest or waiting time ($t_w$)' of the dislocations at the obstacles and the 'ageing time ($t_a$)', i.e., the time required by the diffusing (interstitial) atoms to reach and 'lock' the temporarily stopped dislocations. According to McCormick [24], if $t_w$ is long enough, or in other words $t_w \approx t_a$, the solute atoms can temporarily lock the dislocations and serrated flow may take place. Beukel [25] built up on McCormick's theory and established relations between stress, strain, temperature, and strain rate for the occurrence of DSA. In 1982, Beukel and Kocks [26] discussed the connection between strain rate sensitivity and SSA (static strain aging) and DSA. They proposed that the 'interaction strength' between solutes and dislocations in bcc/fcc interstitial and substitutional alloys varies, and this is why the mechanism of strain aging can be distinct between different alloys. They also calculated the strain rate sensitivity and flow stress in strain aging by taking into account the 'interaction strength'. In 1988, McCormick [27] further added that when the dislocations get pinned by the solute obstacles, there is a local change in the solute

composition at the locked dislocations. He presented constitutive equations that take into account the local change in the composition of the solute atoms during serrated flow to calculate the critical strain for the onset of DSA.

For example in ferritic steels, DSA has been reported to occur at room temperature [28,29] and as well as at temperatures in the range of 80–500 °C [30–33]. The authors [18,28–33] have proposed that the occurrence of DSA in ferritic steels is related to the interaction of dislocations with carbon and/or nitrogen interstitials during the plastic deformation. The presented reasonings agree with the classical theories of DSA [23–27].

In 2011, Lee et al. [34] reported A type DSA serrations in high manganese austenitic twinning induced plasticity (TWIP) steels at room temperature. They explained the occurrence of DSA in the TWIP steels by diffusive jumps of carbon atoms in the Mn–C defect complexes. Jung et al. [35] also reported DSA in TWIP steels and presented a similar explanation as proposed by Lee et al. [34].

DSA in an intercritically annealed TRIP (transformation induced plasticity) steel was observed by Emadoddin et al. [36], and they proposed that in this type of steel SSA and DSA occur due to the difference in the carbon content in bainitic ferrite, polygon ferrite, and retained austenite obtained at different annealing temperatures. However, the specific phase in which strain aging occurs was not specified in this article. Queiroz et al. [37] suggested that in dual phase steels DSA occurs in ferrite and is not affected by the presence of martensite or by carbides in it. DSA in a medium manganese ferritic-austenitic steel was studied by Binhan et al. [38], who observed that in this steel grade the PLC bands are seen in the stress strain curves at almost the same instant when austenite is transformed to martensite. Although they did not provide an explanation for the stated relation between DSA and the TRIP effect, they proposed that the difference in the austenite stability (due to the variation in the C and Mn contents at the intercritical annealing temperatures) might affect the martensite transformation kinetics. Wang et al. [39] investigated the appearance of Luder's and PLC bands in an intercritically annealed medium manganese TRIP steel. Their study showed that much of the transformation from austenite to martensite occurs in the Luder's band and very little of the TRIP effect takes place in the PLC bands. The work of Callahan et al. [40,41] on intercritically annealed 5% Mn TRIP steel, in turn, showed that DSA serrations and the TRIP effect occur at similar strain values in a uniaxial tensile test. They also proposed that the occurrence of the PLC bands is related to austenite stability and that the PLC bands can nucleate and propagate without martensite transformation. The effect of dislocation densities on the unstable plastic flow was investigated by Han et al. [42] using a 7% Mn steel undergone intercritical annealing. They proposed that discontinuous yielding takes place in globular ferrite because of its low dislocation density. Wang et al. [43] also proposed that the difference in the dislocation densities leads to heterogenous plastic flow, and that this applies to both bcc and fcc phases in a multiphase steel. From the above results and claims, it can be summarized that the origin of DSA in multiphase steels is still rather poorly understood at the microscopic level.

The mechanism(s) of DSA have been studied for example, in Al–Mg alloys [17,44] and Au–Cu alloys [45], but the corresponding studies on steels remain rather scarce. The studies on steels have mostly focused on the phenomenological explanation of DSA at varying temperatures and strain rates [18,46,47], but a few studies have tried to explain the DSA phenomena also in steels at the atomic level [29,33]. The current research work focuses on the occurrence of DSA in an intercritically annealed and Q&P heat treated low carbon high aluminum medium manganese steel at low strain rates at room temperature. This article, in turn, concentrates mainly on the questions related to the selection and effects of the Q&P parameters on the DSA phenomena in the studied steel grade.

### 1.1. Methods and materials

The steel grade used in this work is a low carbon high aluminum manganese steel, the chemical composition of which in weight percent is given in Table 1. The steel was vacuum melted in an induction furnace as slabs with a thickness of 55 mm. The slabs were homogenized at 1250 °C for 2 h, followed by hot rolling. The steel was hot rolled to 3 mm thickness with a reduction of approximately 30%, and the finish rolling temperature (FRT) was 880 °C. The slabs were slowly cooled to room temperature inside the furnace. The samples were then cold rolled to 1.5 mm thickness with 50% reduction and cut into bars with dimensions of 10 × 100 mm. The cutting direction was transverse to the rolling direction.

### 1.2. Quench and partition treatments

Different quench and partition treatments were performed on cold rolled 10 × 100 mm bars, starting from the intercritical annealing temperatures of 820 °C, 780 °C and 740 °C, which correspond to the austenite fractions of approximately 60%, 50% and 40%. The calculated $A_1$ and $A_3$ temperatures of the steel were 717 °C and 914 °C, respectively. The volume fractions of austenite at the intercritical annealing temperatures and the phase transformation temperatures $A_1$ and $A_3$ were determined using the CALPHAD JMatPro® (version 12.4) software. The quench temperatures were estimated using the Speer's method [4]. The athermal progression of the austenite transformation to martensite was calculated using the Lee-Van-Tyne equation [48], and the $M_s$ temperature using the Capdevila's equation [49]. The Speer's method for estimating the optimal retained austenite fraction [4] can be used for fully austenitized as well as for intercritically annealed specimens. According to Refs. [2,50], the Speer's method/model can also be used for intercritically annealed samples, provided that the initial carbon content in the austenite at the intercritical annealing temperature is used in the model. In this work, the quench stop temperatures (in the conducted Q&P heat treatments) were calculated using the initial carbon content in the austenite at the partial annealing temperatures. The initial carbon content in the austenite at 820 °C was 0.39 wt%, at 780 °C 0.49 wt%, and at 740 °C 0.61 wt%. Also for the determination of the carbon contents of austenite, JMatPro® was used. The results obtained with the Speer's method for optimal quench temperatures are presented in Fig. 2, based on which 175 °C and 200 °C were selected as quench stop temperatures for the Q&P heat treatments. The reason for using these two quench temperatures was to study the microstructures and properties when quenching took place also to the temperatures on the 'low' and 'high' sides of the optimal quench temperature curves presented in Fig. 2. From Fig. 2, it can be seen that both quench temperatures for the sample annealed at 740 °C are on the 'high' side of the optimal quench temperature curve, for the sample annealed at 780 °C at the 'optimum' (i.e., producing the highest amount of retained austenite) as well as on the 'low' side of the optimal quench temperature curve, and for the sample annealed at 820 °C on the 'low' side of the respective quench temperature curve. The selected partition temperature was in all cases 400 °C, whereas the partition took place for 30, 90 or 300 s.

The Q&P heat treatments were conducted at the laboratory of Materials Science and Engineering of Tampere University. An austenitizing furnace and two salt bath furnaces were used to carry out the heat treatments. One of the salt bath furnaces was used for quenching to 175 °C or 200 °C for 5 s, and the other salt bath furnace for partitioning at 400 °C for 30, 90 or 300 s, as presented in Fig. 3. Altogether eighteen different Q&P treatments (with sample codes and processing parameters

**Table 1**
Chemical composition of the investigated alloy in weight percent.

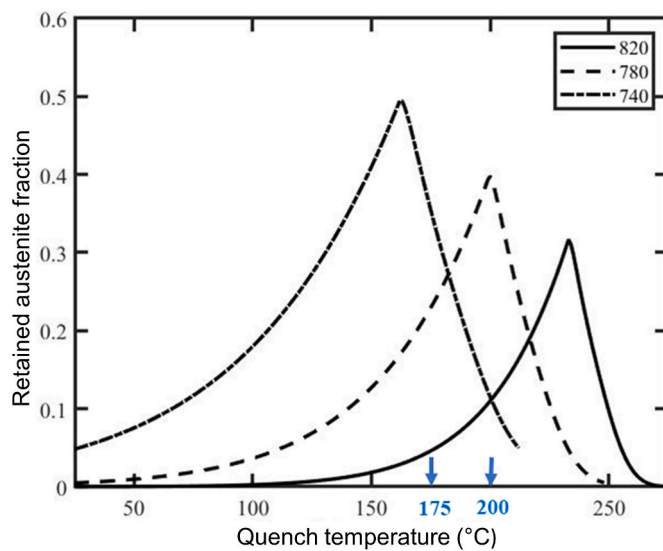| Element | C | Al | Si | Mn | Mo | Cr | Cu |
|---------|------|------|------|-----|------|------|------|
| Wt% | 0.26 | 1.35 | 0.85 | 3.0 | 0.41 | 0.02 | 0.01 |

**Fig. 2.** Results of the application of the Speer's method for finding the optimal quench temperature, calculated for the intercritical annealing temperatures of 820 °C, 780 °C and 740 °C. 175 °C and 200 °C (marked with blue arrows in the graph) are the temperatures selected for the quench-stop temperatures used in the Q&P treatments. (For interpretation of the references to color in this figure legend, the reader is referred to the Web version of this article.)

presented in Table 2) were conducted. The aim was to study the mechanical properties and phase compositions produced by each of the above thermal treatments.

The 100 mm long heat treated bars were cut into two rectangular pieces with lengths of 40 mm and 60 mm. The 60 mm long pieces were used for preparing tensile test specimens, while the 40 mm long pieces were used for microstructural characterizations.

### 1.3. Characterization of the heat-treated samples

The volume fractions of retained austenite in the Q&P treated samples were determined by X-ray diffraction using Panalytical Empyrean X-ray Diffractometer (XRD, Malvern Panalytical Ltd., UK). The retained austenite fractions were calculated using the four peak method according to standard SP-453 [51] with a cobalt cathode ($40° < 2θ < 130°$) operated at 40 KV and 45 mA and a 0.013° step size with 80 s time per step. The carbon content in austenite was calculated using the Dyson and Holmes equation [52]. The samples used for XRD were first coarse ground with a 800 grit SiC paper, then fine ground with a 4000 grit SiC

paper, and finally electropolished using Struers® LectroPol-5 with A2 as an electrolyte.

The microstructural analysis of the heat-treated samples was conducted using Zeiss ULTRAplus field emission scanning electron microscope (FESEM). The SEM samples were prepared with the same metallographic sample preparation method as for XRD, with the only exception that instead of electropolishing, the samples were polished using diamond suspensions with decreasing sizes of 6 μm, 3 μm, 1 μm, and the final polishing was done using colloidal silica suspension. Before SEM observations, the samples were etched with 2% nital.

Crystallographic and phase analyses of the samples were conducted using Oxford Instruments Symmetry® electron backscatter diffraction (EBSD) detector. The EBSD samples were cut directly from the heat-treated specimens and prepared using JEOL IB-19530 cross section polisher. The ion beam accelerating voltage was 6.0 KV, and the polishing time was 3 h. Additional polishing was conducted at 3.0 KV for 45 min. Some samples for EBSD were prepared by mechanical grinding, and the final polishing was done using colloidal silica. The EBSD data for all samples was acquired using an accelerating voltage of 15 KV, working distance of 12 mm, magnification of 5000×, and step size of 40 nm or in some cases 25 nm.

Transmission electron microscopy (TEM) analysis was conducted using JEOL JEM-F200 TEM working at 200 KV acceleration voltage. The TEM samples were first mechanically ground to the thickness of 80 μm, and then electrolytically polished using Struers® Tenupol-5 electrolytic polisher operating at 32 V. The electrolyte used in the polishing was A2, and the working temperature was 263 K (−10 °C).

### 1.4. Tensile testing

Tensile specimens with a gauge length of 15 mm and a gauge width of 4 mm were prepared from the 60 mm long heat-treated bars using an automated milling machine. The mechanical properties of the test materials were determined using an Instron 8800 uniaxial servo-hydraulic materials testing machine. In the tensile tests, the direction of loading was transverse to the direction of rolling. The strain rate in the tests was $0.00025\ s^{-1}$, which corresponds to a constant piston speed of approximately 0.225 mm/min. For strain measurement, a LaVision SMC 5M − 140 optical extensometer with Davis software for digital image correlation (DIC) was used. The frame rate in the image recording was 2 Hz, and the strain calculation was based on either a $9 × 9$ or a $11 × 11$ subset, with a step size of 1. Strain was calculated by Davis software for every frame relative to the first frame acquired. With the used setup, the gauge length was about 300 pixels long and the width of the sample was 70 pixels, one pixel corresponding to about 52 μm. For a couple of samples, mechanical extensometer was also used for obtaining the
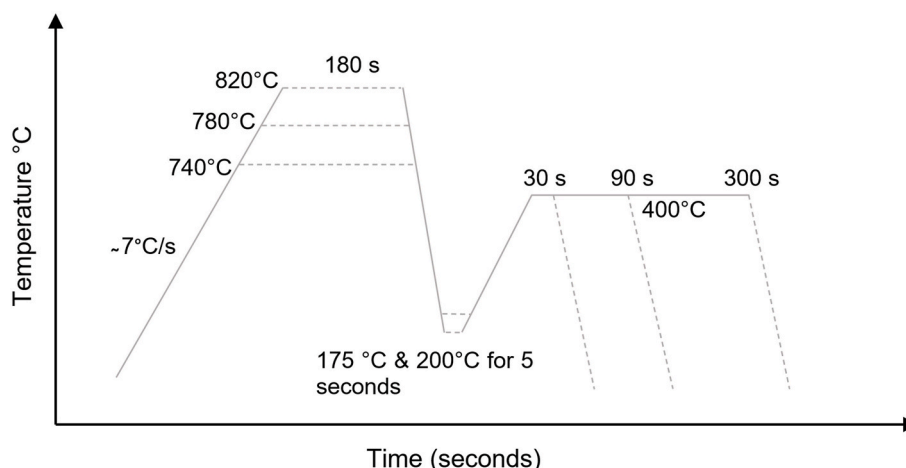


**Fig. 3.** Heat treatment cycles used for the Q&P heat treatments in the current work.

**Table 2**
Sample names and processing parameters of the Q&P heat treatments.

| Sample name | Annealing temperature (°C) | Annealing time (seconds) | Quench temperature (°C) | Partitioning temperature (°C) | Partitioning time (seconds) |
|---|---|---|---|---|---|
| 1.1 | 740 | 180 | 175 | 400 | 30 |
| 1.2 | 740 | 180 | 175 | 400 | 90 |
| 1.3 | 740 | 180 | 175 | 400 | 300 |
| 1.4 | 780 | 180 | 175 | 400 | 30 |
| 1.5 | 780 | 180 | 175 | 400 | 90 |
| 1.6 | 780 | 180 | 175 | 400 | 300 |
| 1.7 | 820 | 180 | 175 | 400 | 30 |
| 1.8 | 820 | 180 | 175 | 400 | 90 |
| 1.9 | 820 | 180 | 175 | 400 | 300 |
| 2.1 | 740 | 180 | 200 | 400 | 30 |
| 2.2 | 740 | 180 | 200 | 400 | 90 |
| 2.3 | 740 | 180 | 200 | 400 | 300 |
| 2.4 | 780 | 180 | 200 | 400 | 30 |
| 2.5 | 780 | 180 | 200 | 400 | 90 |
| 2.6 | 780 | 180 | 200 | 400 | 300 |
| 2.7 | 820 | 180 | 200 | 400 | 30 |
| 2.8 | 820 | 180 | 200 | 400 | 90 |
| 2.9 | 820 | 180 | 200 | 400 | 300 |

stress-strain data.

## 2. Results and discussions

The tensile test results and mechanical properties for selected samples (intercritically annealed at 780 °C and 820 °C) are presented in Fig. 4 and Table 3. The retained austenite fractions and carbon contents of the samples acquired with XRD are, in turn, presented in Table 4. From Fig. 4, it is evident that the samples that were intercritically annealed at 820 °C (samples 1.8 and 2.8) possess higher strength and larger elongation than the samples annealed at the lower temperature of 780 °C. The XRD data shown in Table 4 reveals that the fraction of retained austenite as well as its carbon content are lower in the samples annealed at 820 °C. The EBSD micrographs of samples 2.5 and 2.8 are also depicted with their respective stress-strain curves in Fig. 4. The EBSD data of sample 2.5 reveals the presence of blocky as well as lath retained austenite, while sample 2.8 contains mainly lath retained austenite. Also, the fractions of recrystallized ferrite and martensite in sample 2.8 are higher compared to sample 2.5. The higher strength of
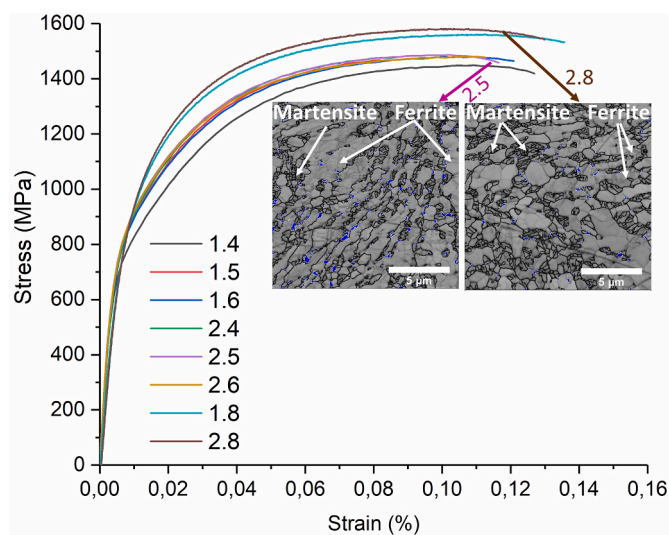


**Fig. 4.** Stress-strain curves of the Q&P heat treated samples intercritically annealed at 820 °C and 780 °C and subsequent distribution of retained austenite (EBSD band contrast maps overlaid with FCC phase maps, blue color represents FCC phase and black lines are BCC grain boundaries) of samples 2.5 and 2.8. (For interpretation of the references to color in this figure legend, the reader is referred to the Web version of this article.)

**Table 3**
Mechanical properties of selected Q&P samples intercritically annealed at 820 °C and 780 °C.

| Sample | Yield strength MPa | Ultimate tensile strength MPa | Uniform Elongation (%) | Total Elongation (%) |
|---|---|---|---|---|
| 1.4 | 700 | 1450 | 10.9 | 12.7 |
| 1.5 | 765 | 1465 | 7.97 | 8.2 |
| 1.6 | 800 | 1480 | 10.9 | 12.1 |
| 1.8 | 875 | 1560 | 11.26 | 13.5 |
| 2.4 | 800 | 1475 | 8.24 | 8.7 |
| 2.5 | 830 | 1486 | 10.23 | 11.6 |
| 2.6 | 820 | 1480 | 11.0 | 11.2 |
| 2.8 | 855 | 1582 | 10.7 | 12.9 |

**Table 4**
The fraction and carbon content of retained austenite in selected Q&P heat treated samples intercritically annealed at 780 °C (samples 1.4–1.6 and 2.4–2.6) and 820 °C (samples 1.8 and 2.8) with the respective quench temperatures and partition times.

| Sample | 1.4 | 1.5 | 1.6 | 1.8 | 2.4 | 2.5 | 2.6 | 2.8 |
|---|---|---|---|---|---|---|---|---|
| Quench temperature (°C) | 175 | 175 | 175 | 175 | 200 | 200 | 200 | 200 |
| Partition time (s) | 30 | 90 | 300 | 90 | 30 | 90 | 300 | 90 |
| Retained austenite fraction (%) | 11.8 | 29.0 | 27.4 | 5.8 | 8.7 | 10.9 | 12.0 | 7.0 |
| C content in austenite (%) | 1.01 | 1.11 | 1.11 | 0.96 | 1.00 | 1.01 | 1.01 | 1.02 |

samples 1.8 and 2.8 can be explained by their higher martensite contents, and a probable reason for their higher elongation is the presence of mainly lath type retained austenite, whose mechanical stability is higher than that of the blocky type austenite [9,10,53].

The tensile test results for the specimens intercritically annealed at 740 °C are shown in Fig. 5. The key mechanical properties of these samples, determined from the observed stress-strain curves, are presented in Table 5.

When comparing Figs. 4 and 5, it can be noticed that none of the samples annealed at 820 °C and 780 °C shows any (type of) DSA serrations, while all samples annealed at 740 °C exhibit DSA serrations of either type A or type D. From here on, the focus of this article is directed towards the samples that showed DSA serrations in the tensile tests, i.e., the samples annealed at 740 °C (1.1, 1.2, 1.3, 2.1, 2.2 and 2.3).

In Fig. 5, two different types of DSA serrations can be observed; in
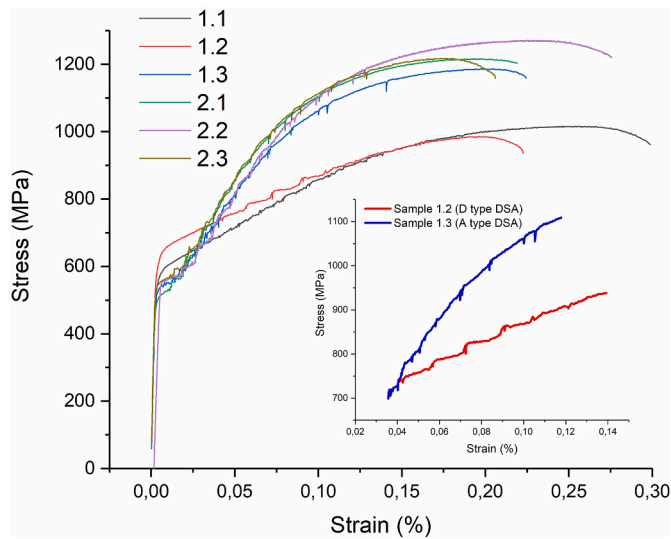
**Fig. 5.** Stress-strain curves of the investigated samples intercritically annealed at 740 °C, and a close-up of tensile curves of samples 1.2 and 1.3 depicting type D type and type A DSA serrations, respectively.



**Fig. 6.** Association of the DIC images with the stress-strain curve of sample 1.3.

**Table 5**
Summary of the mechanical properties of selected Q&P samples intercritically annealed at 740 °C.

| Sample | Yield strength MPa | Ultimate tensile strength MPa | Uniform Elongation (%) | Total Elongation (%) |
|--------|--------|--------|--------|--------|
| 1.1 | 590 | 1015 | 25.3 | 29.8 |
| 1.2 | 634 | 986 | 19.5 | 22.2 |
| 1.3 | 544 | 1186 | 20.4 | 22.5 |
| 2.1 | 514 | 1217 | 19.3 | 22.8 |
| 2.2 | 535 | 1272 | 18.0 | 22.1 |
| 2.3 | 541 | 1218 | 17.3 | 20.5 |

sample 1.2, the serrations are clearly of type D, while the serrations in samples 1.3, 2.1, 2.2 and 2.3 are of the A type. Comparison of Fig. 5 with Fig. 1 confirms that type A DSA serrations, i.e., definite sudden load drops, are associated with otherwise rather high work hardening rate of the steel, while D type DSA serrations are characterized by a much lower overall work hardening rate and almost non-hardening 'plateaus' in the stress-strain curve, as seen especially for sample 1.2. The behavior of sample 1.1 is also characterized by a relatively low work hardening rate, but the serrations do not form clear 'steps' and may therefore not be categorized as type D DSA serrations. As mentioned in Chapter 1, the DSA effects in steels can be rather complex, which makes it possible that two different DSA mechanisms are occurring simultaneously in sample 1.1, making identification/classification of the DSA type more difficult.

The digital camera images of sample 1.3 are correlated with the stress-strain curve in Fig. 6. The DIC images are associated with the stress-strain curve (showing A type DSA serrations) for better correlation with the changes occurring in the sample during straining and work hardening. From Fig. 6, it can be seen that the first bands that nucleate right after the yield point are typical Luder's bands, caused by static strain aging (SSA). When the strain hardening stage commences, progressive nucleation and propagation of PLC bands are seen with increasing strain values. The PLC bands also appear to propagate always in the same direction, i.e., from the same end of the specimen to the other end, which is a typical characteristic of type A DSA serrations [18]. The nucleation of the next set of deformation bands occurs after the previous bands have reached the other ('far') end of the gauge length. The stress drops that are seen at higher strains in Fig. 6 as A type DSA serrations seem to coincide with the bands reaching the end of the gauge
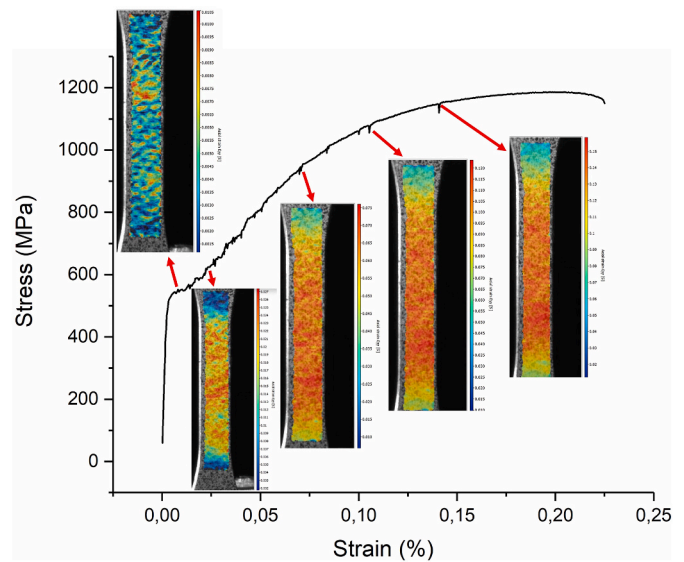
length, but this observation still needs to be verified with more precise measurements for example by increasing the sampling rates of stress (load) and strain (digital imaging rate) considerably.

The fraction of retained austenite and the carbon content in the austenite were determined by XRD, as shown in Table 6. The analyzed peaks for ferrite were (110), (200), (211) and (220), while the analyzed peaks for austenite were (111), (200), (220) and (311). The EBSD phase maps for the Q&P heat treated samples 1.1 and 1.2 are, in turn, shown in Fig. 7. These samples (in Fig. 7) were prepared by ion milling with parameters given in section 1.3.

Based on the EBSD investigations, it is evident that little to no martensite was formed during the quenching in any of the two samples presented in Fig. 7. Instead, their microstructure mainly consists of ferrite and blocky retained austenite only. Comparison of the XRD data presented in Tables 4 and 6 shows that the carbon content in the austenite phase of samples annealed at 740 °C (1.1–1.3 and 2.1 to 2.3) is high compared to the samples intercritically annealed at 780 °C and 820 °C, which is the probable reason why sufficient blocky austenite is retained at room temperature in the samples annealed at 740 °C. The XRD data in Table 6 also shows that the fraction of retained austenite in samples quenched to 175 °C (1.1, 1.2 and 1.3) has a clear maximum or 'peak value' when the partitioning time at 400 °C is 90 s, while the samples quenched to 200 °C (2.1, 2.2 and 2.3) show similar amounts of austenite with almost the same carbon content irrespective of the partitioning time. The varying ('peaking') contents of retained austenite in samples 1.1 through 1.3 can be explained by the progression of the carbon partitioning process. In sample 1.1, the partitioning time of 30 s is not long enough to stabilize a sufficient amount of retained austenite and the sample may still contain a small amount of martensite, from which carbon did not yet sufficiently partition to austenite. For sample 1.2, it seems that most carbon has partitioned into austenite and there is little to no martensite left in the sample. The again small amount of

**Table 6**
The fraction and carbon content of retained austenite in the Q&P treated samples intercritically annealed at 740 °C, with respective quench temperatures and partition times.

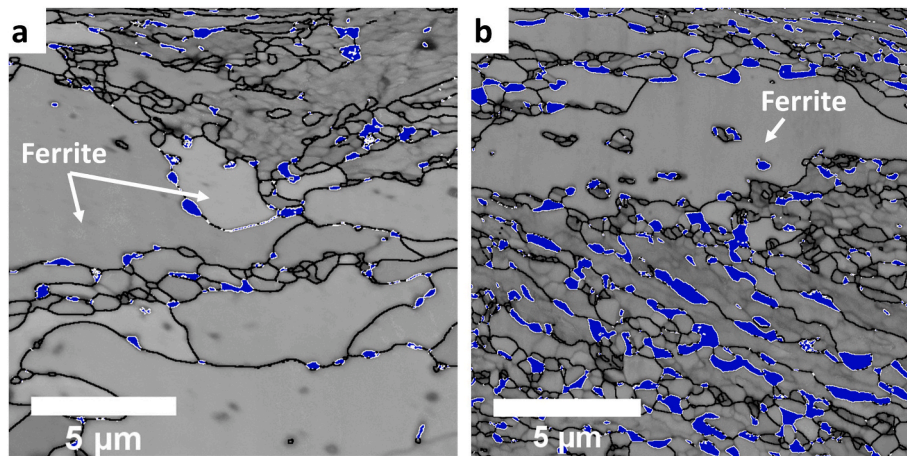| Sample | 1.1 | 1.2 | 1.3 | 2.1 | 2.2 | 2.3 |
|--------|-----|-----|-----|-----|-----|-----|
| Quench temperature (°C) | 175 | 175 | 175 | 200 | 200 | 200 |
| Partition time (s) | 30 | 90 | 300 | 30 | 90 | 300 |
| Retained austenite fraction (%) | 5.8 | 34.1 | 7.7 | 33.4 | 31.9 | 31.0 |
| C content in austenite (%) | 1.26 | 1.19 | 1.26 | 1.20 | 1.20 | 1.19 |

**Fig. 7.** EBSD band contrast maps overlaid with FCC phase maps (blue color represents the FCC phase and black lines are the BCC grain boundaries) (a) sample 1.1 (b) sample 1.2. (For interpretation of the references to color in this figure legend, the reader is referred to the Web version of this article.)

retained austenite in sample 1.3 can be explained by the presence of small amount of fresh martensite, i.e., instead of partitioning to retained austenite and stabilizing it, partitioning carbon has led to the formation of secondary or fresh martensite. For the samples 2.1 through 2.3 (quenched to 200 °C), the XRD data shows that almost all carbon has partitioned to austenite at the Q&P annealing temperature and there is no primary nor secondary martensite present in the microstructures of these samples. The microstructures presented in Fig. 7 also indicate that the entire Q&P process has not taken place properly because the Q&P heat treatment requires the formation of sufficient martensite at the quench stop temperatures so that carbon partitioning from martensite to austenite during the partition stage can take place [2,3]. Furthermore, the EBSD micrographs in Fig. 7 reveal the nucleation of austenite at the ferritic boundaries, which suggests that the intercritical annealing temperature has been (too) close to the $A_1$ transformation temperature. The obvious reason for the absence of martensite is that the calculated $M_s$ temperature for the studied steel grade annealed at 740 °C was not accurate and should be corrected for. A probable solution might be to substitute the entire intercritical annealing composition in the $M_s$ temperature equations instead of just substituting the carbon values. The intercritical annealing compositions can be calculated for example with a CALPHAD software, such as JMatPro®.

Comparison of the micrographs presented in Fig. 7 for samples that showed DSA serrations with the micrographs presented in Fig. 4 for samples that did not show any signs of DSA, reveals some differences in the microstructures. The microstructures of the samples intercritically annealed at 740 °C (Fig. 7) contain large fractions of ferrite (including recrystallized ferrite) and blocky retained austenite along the ferrite grain boundaries but little to no martensite, while the microstructures of samples 2.5 and 2.8 (Fig. 4) contain less retained austenite (with mainly lath morphology) along with ferrite and some amount of martensite.

In austenite-containing multiphase steels, deformation induced transformation of austenite to martensite has been reported to cause serrations in the stress-strain curves during deformation at room temperature [38,40,41,54]. The proposed reason for this occurrence is related to the change in the RT stability of austenite caused by the changes in its chemical composition at different intercritical annealing temperatures, i.e., the contents of C and Mn in austenite changes as the intercritical annealing temperature is changed. This change in the chemical composition of austenite causes unstable TRIP effect and eventually leads to jerky flow. Unstable plastic deformation due to the change in the stability of austenite has also been reported by Gibbs et al. [55] and Ryu et al. [56], although the reason for the heterogenous plastic flow was not presented. A probable reason for the occurrence of DSA in the fcc structure at room temperature was put forward by Lee

et al. [34], but the investigation was conducted on high manganese TWIP steels. From Fig. 7 it can be seen that considerable fractions of retained austenite are present at room temperature in the samples that show DSA serrations. So, the jerky flow observed in the investigated samples may also be due to the retained austenite undergoing the TRIP transformation, and for example, the authors of [38,40,41] have associated jerky flow to the nucleation of PLC bands during the unstable TRIP effect. However, further experimental evidence and studies are required to prove the relation between the PLC bands and the TRIP transformation. An interesting feature to note in the investigated microstructures is the distinct morphology of retained austenite. By comparing the EBSD micrographs presented in Figs. 7 and 4, it can be seen that blocky morphology of retained austenite is seen in the samples that show DSA serrations, while mainly lath morphology is seen in samples 2.5 and 2.8 (Fig. 4) that did not show any DSA serrations. Some studies show that the stability of retained austenite depends on the morphology [9,53], so it might be possible that the morphology of retained austenite also affects the occurrence of the (DSA) serrations. Studies related to DSA serrations and the morphology of retained austenite have not been reported in the literature and would therefore be an interesting subject of a further study.

Previous studies on multiphase steels have proposed that SSA and DSA take place primarily in the phase(s) with a bcc structure [37,39,42, 43] and that the reasons for the occurrence of DSA serrations include the difference in the dislocation density in the ferrite grains [39,42,43] and the interaction of interstitial solute atoms with dislocations [37]. In the current study, however, it is not clear how (and to what extent) the different microstructures are involved in causing the DSA serrations at the atomic scale in the samples of aluminum alloyed 3% manganese steels partially annealed at different temperatures.

To further understand the difference between the samples that showed DSA serrations (1.1, 1.2, 1.3, 2.1, 2.2 and 2.3) and the samples that did not show them (e.g., sample 1.5), TEM investigations on selected samples were conducted before and after tensile testing. The TEM micrographs of the samples before tensile testing are presented in Fig. 8, showing that samples 1.2 and 2.1 contain carbides in their microstructure. The carbides, the size of which ranges from 80 to 160 nm, are mostly spherical in shape and appear to reside inside the ferrite phase. The TEM micrograph from sample 1.5 (Fig. 8c) that did not show DSA serrations, instead, does not contain any carbides. As the precipitation of carbides is generally assumed to inhibit DSA serrations [46, 57–59] rather than to promote them, their existence may not be expected to be directly the reason for the observed DSA serrations either in this case.

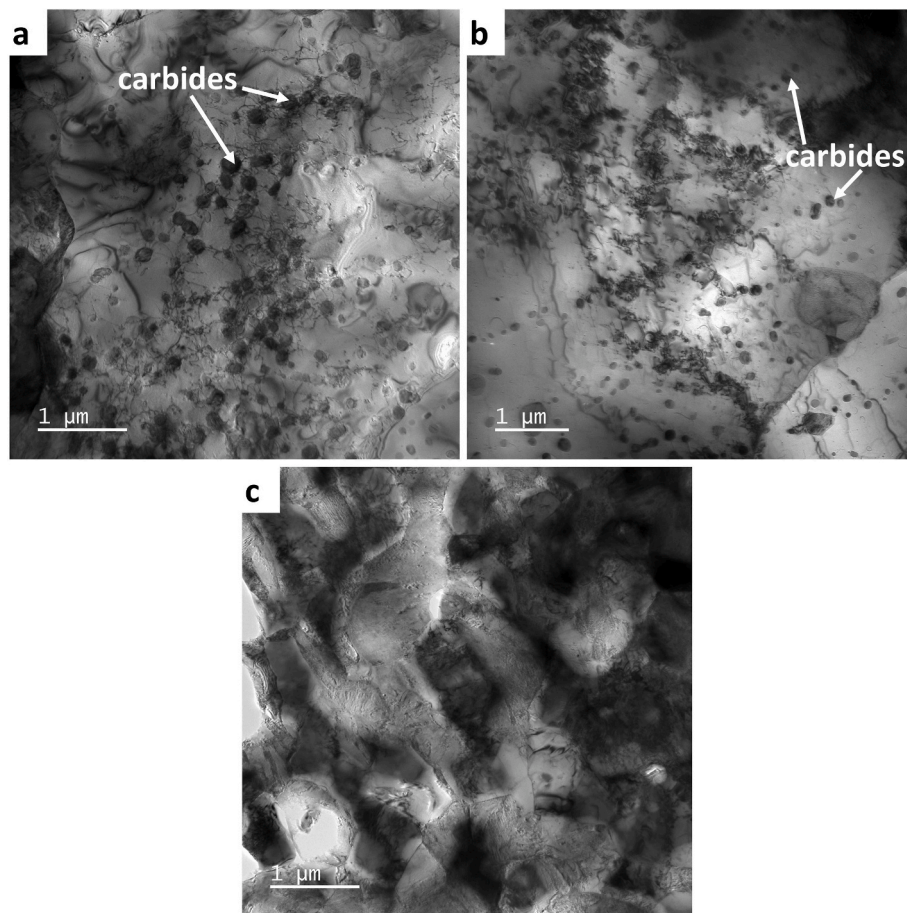To examine the formation and nature of the carbides, additional

**Fig. 8.** TEM micrographs of samples before tensile testing (a) 1.2 (b) 2.1 (c) 1.5 (no carbides observed).

quenching heat treatment experiments were conducted. Samples of the studied steel grade were partially austenitized at different intercritical annealing temperatures, followed by direct water quenching to room temperature. The purpose of these experiments was to determine whether the carbides are forming at the intercritical annealing temperature or later at some stage during the Q&P treatment. The selected annealing temperatures were, 740 °C, 750 °C, 760 °C and 780 °C. SEM micrographs of the samples that were quenched to room temperature
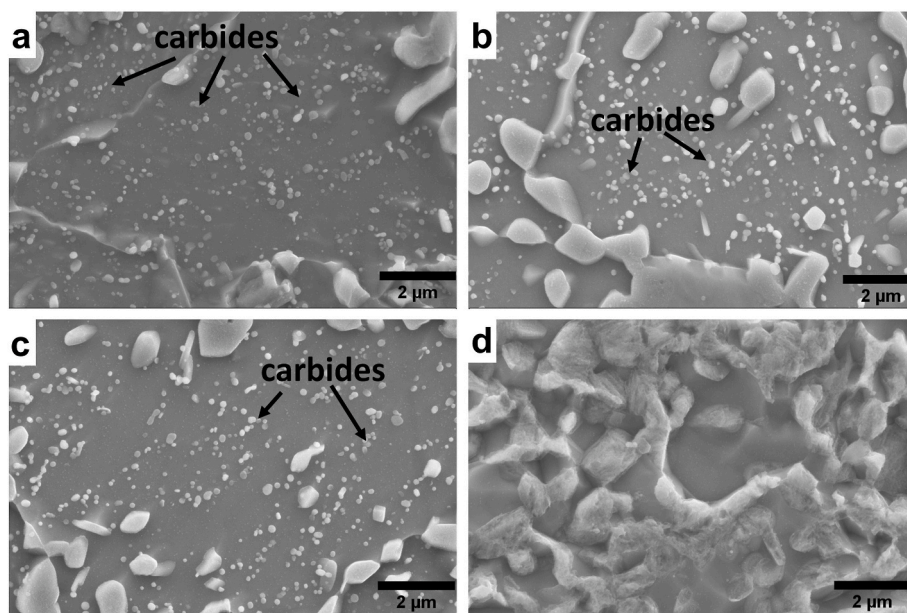


**Fig. 9.** SEM micrographs of samples (a) annealed at 740 °C and quenched to RT, (b) annealed at 750 °C and quenched to RT, (c) annealed at 760 °C and quenched to RT and (d) annealed at 780 °C and quenched to RT. Carbides are observed in all samples except in the one annealed at 780 °C.

after partial austenitization are presented in Fig. 9. The samples that were annealed at 740 °C, 750 °C and 760 °C show the presence of carbides inside ferrite, while the sample partially austenitized at 780 °C does not contain carbides. The observed carbides are also in the same size range as seen in the TEM images presented in Fig. 8a and b. These experiments confirm that the carbides are forming during the partial austenitization temperature but only below 780 °C. To investigate more closely the nature of the observed carbides, a JMatPro® simulation was conducted. The simulation results presented in Fig. 10a show that these carbides form when the annealing temperature is between 640 °C and 660 °C and that they start to dissolve in the solid solution when the annealing temperature is above 680 °C. When the temperature reaches 780 °C, they have dissolved completely. The simulation results are in line with the images shown in Fig. 9. According to JMatPro®, the carbides are of type M(C,N) and $M_2$(C,N). The precipitation of these carbides has also been reported by Lee et al. [60], who suggested that the carbides precipitate close to the $A_1$ transformation temperature. The JMatPro® simulation results indicate that the carbides are dissolving during annealing at 740 °C, which means that carbides are freeing carbon and nitrogen inside ferrite during the dissolution process. This might be the reason why DSA is observed in the samples that are annealed at 740 °C, i.e., samples 1.1–1.3 and 2.1–2.3, where the carbides are not completely dissolved in 180 s, which was the annealing time for the samples used in the Q&P treatments. Because the dissolution process is still incomplete at the end of the annealing time, the ferrite phase contains excess amounts of free C and N interstitials, which can easily interact with the moving dislocations and cause DSA serrations. Similar conclusion was presented by Gonzalez et al. [61], who proposed that DSA in pearlitic steels is occurring in ferrite by the interaction of dislocations and C atoms given off upon decomposition of cementite. The speculation presented in this study about the interaction of moving dislocations with the solute atoms originating from the decomposition of carbides and leading to DSA agrees with the theories presented by Cottrell [23], McCormick [24,27] and Beukel [25,26].

A TTT (time temperature transformation) diagram presented in Fig. 10b was also created by using JMatPro®. The diagram indicates that retained austenite is still stable at room temperature after partitioning and that no phase transformation takes place at the partitioning temperature of 400 °C during the partition time of 300 s (which was the maximum partitioning time used in the current Q&P treatments).

To confirm the above findings and to find support for the presented discussion, the samples were examined with TEM also after tensile testing. TEM micrographs of samples 1.2 and 2.1 after tensile testing are presented in Fig. 11. Fig. 11a shows typical dislocation cell walls around the carbides (pointed by blue arrows), which is more or less expected as the dislocations tend to get entangled around the carbides. Another type of regions of interest are pointed by the red arrows, where the dislocation cell walls are further away from the carbides in otherwise quite dislocation free areas. It might be speculated that these are regions where dissolution of the carbides had already occurred, but there are still plenty of free C and N interstitials for dislocations to interact with and cause DSA serrations in the tensile tests. Similar kind of dislocation cell walls are also seen in Fig. 11b, which is taken from sample 2.1. It is quite clear that based on a few TEM images it is not possible to differentiate between the D type DSA serrations exhibited by sample 1.2 and the A type DSA serrations exhibited by sample 2.1, and therefore further investigations must be conducted to gain more insight also into this question.

However, as mentioned before, it is possible that the serrations observed in the tensile test curves of certain types of steels may be due to slightly different kinds of phenomena such as the direct interaction between moving dislocations and the (interstitial) solute atoms (i.e., 'ordinary' dynamic strain aging) in ferrite, or the deformation induced transformation of austenite to martensite in the retained austenite, leading to unstable plastic flow of the material. It may therefore be speculated that more than one mechanism of jerky flow is active in the same multiphase structure, but the mechanisms are very difficult to separate from one another by conventional research methods.

## 3. Conclusions

In this work, the occurrence of dynamic strain aging (DSA) in intercritically annealed Q&P steels with varying heat treatment parameters was investigated. The results highlight the effect of changing Q&P parameters on the mechanical behavior of low carbon medium manganese high aluminum steels. In addition to the tensile tests that exhibited serrations in the stress-strain curves of the samples, the microstructures of the samples that showed serrations were compared with the microstructures of the samples where the serrations were absent. The main results and conclusions of the research work can be summarized as follows:

1. The used Q&P parameters lead to very stable retained austenite at RT, and little to no martensite was formed during the initial quenching stage of the Q&P treatment. That means that changes in the $M_s$ temperature equations must be done to determine the
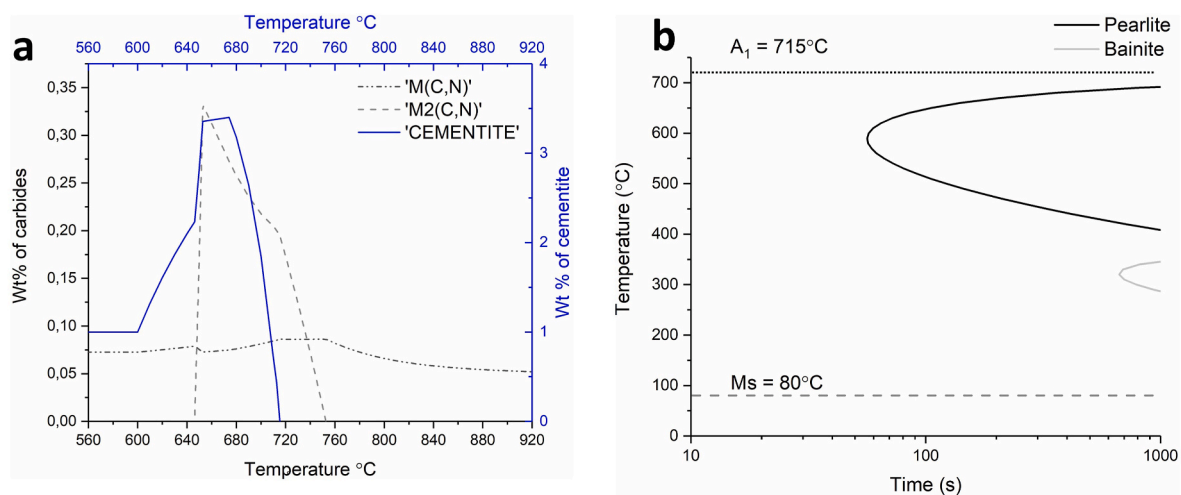


**Fig. 10.** (a) JMatPro® simulation for the presence of carbides at different partial austenitization temperatures, (b) TTT diagram obtained from JMatPro® for the austenitization temperature of 740 °C and annealing time of 180 s, showing that no phase transformation is happening at the partition temperature of 400 °C and in the maximum applied partition time of 300 s.
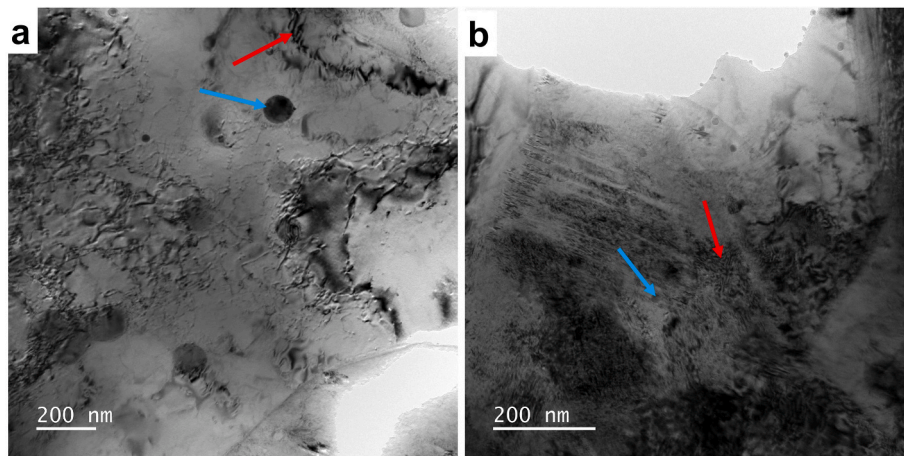
**Fig. 11.** TEM images of the samples showing DSA serrations in the tensile tests; red arrows indicate dislocation walls/cells, and blue arrows indicate carbides, (a) sample 1.2 and (b) sample 2.1. (For interpretation of the references to color in this figure legend, the reader is referred to the Web version of this article.)

optimum Q&P parameters for the samples annealed at 740 °C. An apparent solution is to use the true intercritical austenite composition (at 740 °C) for all elements instead of just adjusting the value of the carbon content.

2. Annealing at close to $A_1$ when the fraction of austenite is close to 40% appears to result in the precipitation of carbides. These carbides are of types M(C,N) and $M_2$(C,N) and enriched with carbon. Dissolution of these carbides occurs between 680 °C and 760 °C, and upon the dissolution, free carbon and nitrogen atoms are present as interstitials in the solid solution. Mobile dislocations can interact with the interstitial atoms, which can result in the build-up of dislocation cell walls. The interactions of the mobile dislocations and interstitial solute atoms can also result in the dynamic strain aging in suitable conditions.

3. Unstable blocky austenite was found in the samples that show serrations in the tensile test curves. It seems possible that this effect is caused by the heterogenous TRIP effect taking place during plastic deformation, as suggested also by some earlier studies. This effect, however, could not be confirmed in this work and further studies are required to understand the relation between the TRIP effect and serrated flow.

4. Type D DSA serrations were observed in one of the samples, but further studies are needed to elucidate the conditions for their occurrence.

### CRediT authorship contribution statement

**Shahroz Ahmed:** Conceptualization, Methodology, Investigation, Software, Writing – original draft. **Jani Penttilä:** Methodology. **Jari Rämö:** Methodology, Investigation. **Mari Honkanen:** Methodology, Investigation. **Veli-Tapani Kuokkala:** Writing – review & editing, Validation, Supervision. **Olli Oja:** Provision of the study materials, Writing – review & editing. **Pasi Peura:** Writing – review & editing, Supervision, Project administration, Validation, Funding acquisition.

### Declaration of competing interest

The authors declare that they have no known competing financial interests or personal relationships that could have appeared to influence the work reported in this paper.

### Data availability

The raw data required to reproduce these findings cannot be shared at this time as the data also forms part of an ongoing study.

### Acknowledgement

### References

[1] L. Liu, B. He, M. Huang, The role of transformation-induced plasticity in the development of advanced high strength steels, Adv. Eng. Mater. 20 (2018) 1–17, https://doi.org/10.1002/adem.201701083.

[2] J.G. Speer, F.C. Rizzo Assunção, D.K. Matlock, D.V. Edmonds, The "quenching and partitioning" process: background and recent progress, Mater. Res. 8 (2005) 417–423.

[3] J.G. Speer, D.K. Matlock, B.C. De Cooman, J.G. Schroth, Carbon partitioning into austenite after martensite transformation, Acta Mater. 51 (2003) 2611–2622, https://doi.org/10.1016/S1359-6454(03)00059-4.

[4] J.G. Speer, A.M. Streicher, D. Matlock, F. Rizzo, G. Krauss, Quenching and Partitioning: A Fundamentally New Process to Create High Strength Trip Sheet Microstructures, Symposium on the Thermodynamics, Kinetics, Characterization and Modelling of: Austenite Formation and Decomposition, 2003, pp. 505–522.

[5] J.G. Speer, E. De Moor, K.O. Findley, D.K. Matlock, B.C. De Cooman, D. V. Edmonds, Analysis of microstructure evolution in quenching and partitioning automotive sheet steel, Metall. and Mater. Trans. A 42 (2011) 3591–3601, https://doi.org/10.1007/s11661-011-0869-7.

[6] J. Sun, H. Yu, Microstructure development and mechanical properties of quenching and partitioning (Q&P) steel and an incorporation of hot-dipping galvanization during Q&P process, Mater. Sci. Eng. A 586 (2013) 100–107, https://doi.org/10.1016/j.msea.2013.08.021.

[7] E. De Moor, D.K. Matlock, J.G. Speer, M.J. Merwin, Austenite stabilization through manganese enrichment, Scripta Mater. 64 (2011) 185–188, https://doi.org/10.1016/j.scriptamat.2010.09.040.

[8] E. De Moor, J.G. Speer, D.K. Matlock, J.H. Kwak, Quenching and partitioning of CMnSi steels containing elevated manganese levels, Steel Res. Int. 83 (2012) 322–327, https://doi.org/10.1002/srin.201100318.

[9] S. Yan, X. Liu, W.J. Liu, T. Liang, B. Zhang, L. Liu, Y. Zhao, Comparative study on microstructure and mechanical properties of a C-Mn-Si steel treated by quenching and partitioning (Q&P) processes after a full and intercritical austenitization, Mater. Sci. Eng. A 684 (2017) 261–269, https://doi.org/10.1016/j.msea.2016.12.026.

[10] R.M. Wu, W. Li, C.L. Wang, Y. Xiao, L. Wang, X.J. Jin, Stability of retained austenite through a combined intercritical annealing and quenching and partitioning (IAQP) treatment, Acta Metall. Sin. 28 (2015) 386–393, https://doi.org/10.1007/s40195-015-0217-9.

[11] R. Wu, X. Jin, C. Wang, L. Wang, Effect of intercritical annealing on microstructural evolution and properties of quenched & partitioned (Q&P) steels, J. Mater. Eng. Perform. 25 (2016) 1603–1610, https://doi.org/10.1007/s11665-016-1985-8.

[12] T. Nyyssönen, O. Oja, P. Jussila, A. Saastamoinen, M. Somani, P. Peura, Quenching and partitioning of multiphase aluminum-added steels, Metals 9 (2019) 1–17, https://doi.org/10.3390/met9030373.

[13] T. Nyyssönen, P. Peura, E. De Moor, D. Williamson, V.T. Kuokkala, Crystallography and mechanical properties of intercritically annealed quench and partitioned high-aluminum steel, Mater. Char. 148 (2019) 71–80, https://doi.org/10.1016/j.matchar.2018.12.004.

[14] E.J. Seo, L. Cho, B.C. De Cooman, Application of quenching and partitioning processing to medium Mn Steel, Metall. Mater. Trans. A 46 (2015) 27–31, https://doi.org/10.1007/s11661-014-2657-7.

[15] S. Ayenampudi, C.C. Casero, J. Sietsma, M.J. Santofimia, Microstructure evolution during high-temperature partitioning of a medium-Mn quenching and partitioning steel, Materialia 8 (2019), https://doi.org/10.1016/j.mtla.2019.100492.

[16] F. HajyAkbary, J. Sietsma, G. Miyamoto, T. Furuhara, M.J. Santofimia, Interaction of carbon partitioning, carbide precipitation and bainite formation during the Q&P process in a low C steel, Acta Mater. 104 (2016) 72–83, https://doi.org/10.1016/j.actamat.2015.11.032.

[17] Y. Cai, S. Yang, S. Fu, D. Zhang, Q. Zhang, Investigation of Portevin-Le Chatelier band strain and elastic shrinkage in al-based alloys associated with Mg Contents, J. Mater. Sci. Technol. 33 (2016) 580–586, https://doi.org/10.1016/j.jmst.2016.05.012.

[18] T.R. Jacobs, D.K. Matlock, K.O. Findley, Characterization of localized plastic deformation behaviors associated with dynamic strain aging in pipeline steels using digital image correlation, Int. J. Plast. 123 (2019) 70–85, https://doi.org/10.1016/j.ijplas.2019.07.010.

[19] V.V. Gorbatenko, V.I. Danilov, L.B. Zuev, Plastic flow instability : Chernov – Lüders bands and the Portevin–Le Chatelier effect, 62, 2017, pp. 395–400, https://doi.org/10.1134/S1063784217030082.

[20] P. Rodriguez, Serrated plastic flow, Bull. Mater. Sci. 6 (1984) 653–663. https://link.springer.com/article/10.1007/BF02743993.

[21] A. Yilmaz, The Portevin–Le Chatelier effect: a review of experimental findings, Sci. Technol. Adv. Mater. 12 (2011), https://doi.org/10.1088/1468-6996/12/6/063001.

[22] A. Kozlowska, B. Grzegorczyk, M. Morawiec, A. Grajcar, Explanation of the PLC effect in advanced high-strength medium-Mn steels. A review, Materials 12 (2019) 1–14. https://doi.org/10.3390/ma12244175.

[23] A.H. Cottrell, A note on the Portevin-Le Chatelier effect, Mag. J. Sci. 44 (1953) 829–832, https://doi.org/10.1080/14786440808520347.

[24] P.G. McCormick, A model for the Portevin-Le Chatelier effect in substitutional alloys, Acta Metall. 20 (1972) 351–354. https://doi.org/10.1016/0001-6160(72)90028-4.

[25] A.V.D. Beukel, Theory of the effect of dynamic strain aging on mechanical properties, Phys. Stat. Sol(a) 30 (1975) 197–206, https://doi.org/10.1002/pssa.2210300120.

[26] A.V.D. Beukel, U.F. Kocks, The strain dependence of static and dynamic strain-aging, Acta Metall. 30 (1982) 1027–1034, https://doi.org/10.1016/0001-6160(82)90211-5.

[27] P.G. McCormick, Theory of flow localisation due to dynamic strain ageing, Acta Metall. 36 (1988) 3061–3067, https://doi.org/10.1016/0001-6160(88)90043-0.

[28] A.K. Schdev, Dynamic strain aging of various steels, Met. Trans A. V 13A (1982) 1793–1797, https://doi.org/10.1007/bf02647835.

[29] D. Caillard, Dynamic strain ageing in iron alloys: the shielding effect of carbon, Acta Mater. 112 (2016) 273–284, https://doi.org/10.1016/j.actamat.2016.04.018.

[30] A.K. Taheri, T.M. MacCagno, J.J. Jonas, Effect of cooling rate after hot rolling and of multistage strain aging on the drawability of low-carbon-steel wire rod, Metall. Mater. Trans. A. 26A (1995) 1183–1193, https://doi.org/10.1007/BF02670614.

[31] A.K. Taheri, T.M. MacCagno, J.J. Jonas, Dynamic strain aging and the wire drawing of low carbon steel rods, ISIJ Int. 35 (1995) 1532–1540, https://doi.org/10.2355/isijinternational.35.1532.

[32] G.C. Soares, R.R.U. Queiroz, L.A. Santos, Effects of dynamic strain aging on strain hardening behavior, dislocation substructure, and fracture morphology in a ferritic stainless steel, Metall. Mater. Trans. A 51 (2020) 725–739, https://doi.org/10.1007/s11661-019-05574-6.

[33] D. Caillard, J. Bonneville, Dynamic strain aging caused by a new Peierls mechanism at high-temperature in iron, Scripta Mater. 95 (2015) 15–18, https://doi.org/10.1016/j.scriptamat.2014.09.019.

[34] S.J. Lee, J. Kim, S.N. Kane, B.C. De Cooman, On the origin of dynamic strain aging in twinning-induced plasticity steels, Acta Mater. 59 (2011) 6809–6819, https://doi.org/10.1016/j.actamat.2011.07.040.

[35] I.C. Jung, B.C. De Cooman, Temperature dependence of the flow stress of Fe-18Mn-0.6C-xAl twinning-induced plasticity steel, Acta Mater. 61 (2013) 6724–6735, https://doi.org/10.1016/j.actamat.2013.07.042.

[36] E. Emadoddin, A. Akbarzadeh, G.H. Daneshi, Correlation between luder strain and retained austenite in TRIP-assisted cold rolled steel sheets, Mater. Sci. Eng. A. 447 (2007) 174–179, https://doi.org/10.1016/j.msea.2006.10.046.

[37] R.R.U. Queiroz, F.G.G. Cunha, B.M. Gonzalez, Study of dynamic strain aging in dual phase steel, Mater. Sci. Eng. A. 543 (2012) 84–87, https://doi.org/10.1016/j.msea.2012.02.050.

[38] B. Sun, N. Vanderesse, F. Fazeli, C. Scott, J. Chen, P. Bocher, M. Jahazi, S. Yue, Discontinuous strain-induced martensite transformation related to the Portevin-Le Chatelier effect in a medium manganese steel, Scripta Mater. 133 (2017) 9–13, https://doi.org/10.1016/j.scriptamat.2017.01.022.

[39] X.G. Wang, L. Wang, M.X. Huang, Kinematic and thermal characteristics of Lüders and Portevin-Le Châtelier bands in a medium Mn transformation-induced plasticity steel, Acta Mater. 124 (2017) 17–29, https://doi.org/10.1016/j.actamat.2016.10.069.

[40] M. Callahan, A. Perlade, J.H. Schmitt, Interactions of negative strain rate sensitivity, martensite transformation, and dynamic strain aging in 3rd generation advanced high-strength steels, Mater. Sci. Eng. A. 754 (2019) 140–151, https://doi.org/10.1016/j.msea.2019.03.042.

[41] M. Callahan, O. Hubert, F. Hild, A. Perlade, J.H. Schmitt, Coincidence of strain-induced TRIP and propagative PLC bands in Medium Mn steels, Mater. Sci. Eng. A. 704 (2017) 391–400, https://doi.org/10.1016/j.msea.2017.08.042.

[42] J. Han, S.J. Lee, J.G. Jung, Y.K. Lee, The effects of the initial martensite microstructure on the microstructure and tensile properties of intercritically annealed Fe-9Mn-0.05C steel, Acta Mater. 78 (2014) 369–377, https://doi.org/10.1016/j.actamat.2014.07.005.

[43] X.G. Wang, C.H. Liu, B.B. He, C. Jiang, M.X. Huang, Microscopic strain partitioning in Lüders band of an ultra fine-grained medium Mn steel, Mater. Sci, Eng. A 761 (2019), https://doi.org/10.1016/j.msea.2019.138050.

[44] K. Matsuura, T. Nishiyama, S. Koda, Portevin-Le Chatelier effect in aluminium-magnesium alloys, Trans. Japan Inst. Met. 10 (1969) 429–436. https://doi.org/10.2320/matertrans1960.10.429.

[45] A. Wijler, J.S. Van Westrumt, A new type of stress-strain curve and the Portevin-Le Chatelier effect in Au (14 at.% Cu), Acta Metall. 20 (1972) 355–362. https://doi.org/10.1016/0001-6160(72)90029-6.

[46] D.M. Field, D.C. Van Aken, Dynamic strain aging phenomena and tensile response of medium-Mn TRIP Steel, Metall. Mater. Trans. A 49 (2018) 1152–1166, https://doi.org/10.1007/s11661-018-4481-y.

[47] S. Venkadesan, S. Venugopal, P.V. Sivaprasad, P. Rodriguez, Influence of temperature and strain rate on the nature of serrations observed in a 15Cr-15Ni-2.2Mo-Ti modified austenitic stainless steel during tensile testing, Mater. Trans. 33 (1992) 1040–1045. https://doi.org/10.2320/matertrans1989.33.1040.

[48] S.J. Lee, C. Van Tyne, A kinetics model for martensite transformation in plain carbon and low-alloyed steels, Metall. Mater. Trans. A 43 (2011) 422–427, https://doi.org/10.1007/s11661-011-0872-z.

[49] C. Capdevila, F. Caballero, C.G. de Andrés, Determination of Ms temperature in steels: a Bayesian neural network model, ISIJ Int. 42 (2002) 894–902, https://doi.org/10.2355/isijinternational.42.894.

[50] D.V. Edmonds, K. He, F.C. Rizzo, B.C. De Cooman, D.K. Matlock, J.G. Speer, Quenching and partitioning martensite-A novel steel heat treatment, Mater. Sci. Eng. A. (2006) 438–440, https://doi.org/10.1016/j.msea.2006.02.133.

[51] C.F. Jatczak, Retained austenite and its measurement by X-ray diffraction, SAE Trans. 89 (1980) 1657–1676. http://www.jstor.org/stable/44633786.

[52] D.J. Dyson, Effect of alloying additions on the lattice parameter of austenite, J. Iron Steel Inst. 208 (1970) 469–474.

[53] X.C. Xiong, B. Chen, M.X. Huang, J.F. Wang, L. Wang, The effect of morphology on the stability of retained austenite in a quenched and partitioned steel, Scripta Mater. 68 (2013) 321–324, https://doi.org/10.1016/j.scriptamat.2012.11.003.

[54] F. Yang, H. Luo, E. Pu, S. Zhang, H. Dong, On the characteristics of Portevin–Le Chatelier bands in cold-rolled 7Mn steel showing transformation-induced plasticity, Int. J. Plast. 103 (2018) 188–202, https://doi.org/10.1016/j.ijplas.2018.01.010.

[55] P.J. Gibbs, E. De Moor, M.J. Merwin, B. Clausen, J.G. Speer, D.K. Matlock, Austenite stability effects on tensile behavior of manganese-enriched-austenite transformation-induced plasticity steel, Metall. Mater. Trans. A 42 (2011) 3691–3702. https://doi.org/10.1007/s11661-011-0687-y.

[56] J.H. Ryu, J.I. Kim, H.S. Kim, C.S. Oh, H.K.D.H. Bhadeshia, D.W. Suh, Austenite stability and heterogeneous deformation in fine-grained transformation-induced plasticity-assisted steel, Scripta Mater. 68 (2013) 933–936, https://doi.org/10.1016/j.scriptamat.2013.02.026.

[57] J. Chen, Y. Zhang, J.J. Wang, C.M. Liu, S.X. Zhao, Multistage serrated flow behavior of a medium-manganese high-carbon steel, J. Iron Steel Res. Int. 27 (2020) 1064–1072, https://doi.org/10.1007/s42243-019-00343-6.

[58] B.K. Choudhary, K.B.S. Rao, S.L. Mannan, B.P. Kashyap, Serrated yielding in 9Cr-1Mo ferritic steel, Mater. Sci. Technol. 15 (1999) 791–797, https://doi.org/10.1179/026708399101506580.

[59] J. Min, L.G. Hector, L. Zhang, L. Sun, J.E. Carsley, J. Lin, Plastic instability at elevated temperatures in a TRIP-assisted steel, Mater. Des. 95 (2016) 370–386, https://doi.org/10.1016/j.matdes.2016.01.113.

[60] S. Lee, B.C. De Cooman, Effect of the intercritical annealing temperature on the mechanical properties of 10 Pct Mn multi-phase steel, Metall. Mater. Trans. A 45 (2014) 5009–5016, https://doi.org/10.1007/s11661-014-2449-0.

[61] B.M. Gonzalez, L.A. Marchi, E.J. Da Fonseca, P.J. Modenesi, V.T.L. Buono, Measurement of dynamic strain aging in pearlitic steels by tensile test, ISIJ Int. 43 (2003) 428–432, https://doi.org/10.2355/isijinternational.43.428.